CrystEngComm

PAPER

View Article Online
View Journal | View Issue



Cite this: *CrystEngComm*, 2019, **21**, 494

# Metal–organic frameworks based on tetraphenylpyrazine-derived tetracarboxylic acid for electrocatalytic hydrogen evolution reaction and NAC sensing†

Tao Wang, Kun Huang,* Mengni Peng, Xianglin Li, Defang Han, Linhai Jing and Dabin Qin*

A series of metal–organic frameworks (MOFs), namely $\{[Cd(H_2TCPP)]\cdot 2H_2O\}_n$ (**1**), $\{[Pb_2(TCPP)]\}_n$ (**2**), $\{[La(H_2TCPP)]\cdot 3.7H_2O\}_n$ (**3**), $\{[Sr_3(HTCPP)_2]\cdot 6H_2O\}_n$ (**4**), $\{[Ce(HTCPP)]\cdot H_2O\}_n$ (**5**) and $\{[Mn_2(TCPP)]\cdot 2.13H_2O\}_n$ (**6**), are prepared from 2,3,5,6-(4-carboxyl-tetraphenyl)pyrazine ($H_4$**TCPP**) with various metal salts under hydrothermal conditions and are well characterized. The structural analysis shows that compound **1** presents a 2-fold interpenetrating structure, which exhibits a uninodal 4-c net with a $\{6^6\}\{6\cdot6\cdot6\cdot6(2)\cdot6(2)\cdot6(2)\}$ topology. Compound **2** shows a 3-nodal (5,6,11)-connected 3D framework with a point symbol of $\{4^{10}\}\{4^{14}\cdot6\}\{4^{34}\cdot6^{21}\}$. Compound **3** features a (4,8)-connected 3D network built from a binuclear La cluster with a point symbol of $\{4^{16}\cdot6^{12}\}\{4^4\cdot6^2\}_2$. Compound **4** demonstrates a 5-nodal (4,5,6,7,8)-connected network with a $\{4^{10}\cdot6^5\}\{4^{12}\cdot6^9\}\{4^{18}\cdot6^{10}\}\{4^6\}\{4^7\cdot6^3\}$ topology. Compound **5** exhibits a 3D interlocked eight-connected 20-c net with a point symbol of $\{3^{78}\cdot4^{98}\cdot5^{14}\}$, while compound **6** forms a 3,4,4,5,17-connected net with a point symbol of $\{4\cdot5^2\}_2\{4^{32}\cdot5^6\cdot6^{84}\cdot7^4\cdot8^{10}\}\{4^5\cdot5\}\{4^6\}\{4^8\cdot5^2\}$. In addition, almost all the MOFs display significant fluorescence quenching behaviors by the addition of various nitro-aromatic compounds (NACs), especially TNP. More importantly, six new MOFs have been further investigated to evaluate their electrocatalytic activities for the hydrogen evolution reaction (HER). The results demonstrate that all the MOFs exhibit improved performance compared to ligand $H_4$**TCPP** for the HER with the lowest onset overpotential of 244 mV and the smallest Tafel slope of 248 mV $dec^{-1}$, respectively.

Received 1st November 2018,
Accepted 20th November 2018

DOI: 10.1039/c8ce01868e

rsc.li/crystengcomm



## Introduction

Metal–organic frameworks (MOFs) are a new class of crystalline porous materials constructed from metal ions or metal ion clusters and bridging organic linkers *via* hydrothermal synthesis, which have attracted tremendous attention over the last two decades due to their advantages of tunable composition, easy functionalization, accessible metal sites, high drug/gas loading capacity, and good biocompatibility and biodegradability.[1] To date, much effort has been made to explore the applications of MOFs, which were extended to a broad range of fields, such as gas storage and separation, catalysis, drug delivery, sensors, *etc.*[2]

Due to the serious environmental pollution and the crisis of energy depletion, scientists made great efforts to explore clean and sustainable energy carriers as substitutes for fossil fuels.[3] And, hydrogen is considered as one of the ideal alternatives due to its high energy density, zero-emission and non-toxicity.[4] As such, electrocatalysis of the hydrogen evolution reaction (HER) *via* water splitting emerged as a promising approach for chemically offering carbon-free energy and gradually attracted worldwide attention.[5] Since the electrocatalytic HER was firstly reported by Kita in 1966, extensive research efforts have been focused on this topic.[6] Meanwhile, these research findings indicate that the performance of electrocatalysis is generally limited by the active center, conductivity and pore structure of used materials.[7] Up to now, the development of a rapid and efficient method to obtain hydrogen is still highly needed but challenging. One of the promising applications of MOF materials is to use them as electrocatalysts for the HER. In particular, the unique structure of MOFs made them extremely promising precursors/templates for the electrocatalytic HER and great achievements have been made during the last decade. For example,

*Key Laboratory of Chemical Synthesis and Pollution Control of Sichuan Province, School of Chemistry and Chemical Engineering, China West Normal University, Nanchong 637002, P. R. China. E-mail: hkun2017@cwnu.edu.cn, qdbkyl@cwnu.edu.cn*

† Electronic supplementary information (ESI) available. CCDC reference numbers 1845900–1845904 and 1846960 for compounds **1–6**. Crystal data, additional figures, TGA, PXRD, IR spectra, and optical spectra. For ESI and crystallographic data in CIF or other electronic format see DOI: 10.1039/c8ce01868e

some MOF-derived materials exhibited enhanced electrocatalytic performances, which were superior to noble-metal-based electrocatalysts.[8] However, the development of MOF-derived electrocatalysts for the HER is still in its primary stage. Moreover, developing neat MOF-based active materials without conductive additives or other binders for the HER offers challenging issues, which may be ascribed to their poor electrical conductivity.[9] On the other hand, in consideration of the human survival environment and health security, exploitation of functional chemosensors for detecting nitro-aromatic compounds (NACs) that can harm individuals and the environment is of great significance, and much effort has recently been devoted to the development of MOF-based chemosensors for the detection of NACs.[10]

In recent years, we have designed and prepared several porous MOFs that presented fantastic topologies and promising optical properties.[11] In our continuing research on the preparation and application of MOFs, we herein developed a series of MOFs based on a tetraphenylpyrazine-derived tetracarboxylic acid skeleton and evaluated their electrocatalytic properties for the HER and sensing behaviors towards NACs. The results indicated that compounds **2** and **5** exhibited promising electrocatalytic performances for the HER while almost all compounds showed obvious fluorescence quenching to NACs, which may provide a new avenue for exploring MOF materials in electrocatalytic and sensing materials.

# Experimental

### Materials and methods

The tetracarboxyl ligand **$H_4$TCPP** was synthesized using literature methods.[12] All other reagents and solvents commercially available were employed and used without further purification. Elemental analyses were achieved with a Perkin-Elmer 240 elemental analyzer. IR absorption spectra were measured using KBr pellets on a Nicolet 6700 in the range of 400–4000 $cm^{-1}$ (Fig. S1–S6†). Powder X-ray diffraction (PXRD) patterns were obtained using a Dmax/Ultima IV X-ray powder diffractometer and simulated powder X-ray diffraction patterns were obtained based on single-crystal data using the Mercury software package. Thermal analyses were implemented on a Netzsch STA 449 F3 thermal analyzer and the samples were heated at a rate of 20 °C $min^{-1}$ from room temperature to 600 °C under an Ar atmosphere. Nitrogen adsorption isotherms were measured at 77 K by using an Autosorb-IQ gas analyzer. The specific surface area and pore size distribution were calculated using the Brunauer–Emmett–Teller (BET) method. Luminescence spectra for the solid samples and liquid samples were recorded on a Cary Eclipse fluorescence spectrophotometer at ambient temperature. UV-vis spectra were recorded on a PerkinElmer Lambda 35 UV-vis spectrometer. Electrochemical measurements were carried out on a computer controlled CHI-660E electrochemical workstation using a standard three electrode configuration consisting of a glassy carbon electrode (GCE) with a diameter of 3 mm as the working electrode, platinum wire as the counter electrode and Ag/AgCl as the reference electrode in an electrolyte solution of 1.0 M KOH (pH = 14). All measurements were conducted at room temperature unless otherwise stated.

**Synthesis of $\{[Cd(H_2TCPP)]\cdot 2H_2O\}_n$ (1).** A mixture of **$H_4$TCPP** (0.05 mmol, 28.1 mg) and $Cd(NO_3)_2\cdot 6H_2O$ (0.10 mmol, 31 mg) were dissolved in 14 mL of $CH_3CN/H_2O$ (4 : 3) in a 20 mL vial and heated in a Teflon-lined steel bomb at 160 °C for 4 days. Yellow block crystals were collected in 61.0% yield (based on $H_4$TCPP). Anal. calcd. for $C_{32}H_{16}CdN_2O_{10}$ (%): C, 54.84; H, 2.30; N, 4.00. Found (%): C, 54.90; H, 2.36; N, 4.12%. IR (KBr, $cm^{-1}$): 3416.39 (s), 1580.27 (s), 1541.81 (s), 1387.96 (s), 1096 (w), 1110.03 (m), 856.19 (m).

**Synthesis of $\{[Pb_2(TCPP)]\}_n$ (2).** A mixture of **$H_4$TCPP** (0.05 mmol, 28.1 mg) and $Pb(NO_3)_2$ (0.10 mmol, 22 mg) were dissolved in 14 mL of $CH_3CN/H_2O$ (4 : 3) in a 20 mL vial and heated in a Teflon-lined steel bomb at 160 °C for 4 days. Colorless crystals were collected in 53.0% yield (based on $H_4$-TCPP). Anal. calcd. for $C_{32}H_{16}N_2O_8Pb_2$ (%): C, 39.51; H, 1.86; N, 2.88. Found (%): C, 39.53; H, 1.88; N, 2.92%. IR (KBr, $cm^{-1}$): 3735.79 (w), 3474.92 (m), 1638.80 (m).

**Synthesis of $\{[La(H_2TCPP)]\cdot 3.7H_2O\}_n$ (3).** A mixture of **$H_4$TCPP** (0.05 mmol, 28.1 mg) and $La(NO_3)_3$ (0.10 mmol, 15 mg) were dissolved in 14 mL of $CH_3CN/H_2O$ (4 : 3) in a 20 mL vial and heated in a Teflon-lined steel bomb at 160 °C for 4 days. Colorless crystals were collected in 48.0% yield (based on $H_4$TCPP). Anal. calcd. for $C_{32}H_{19}LaN_2O_{11.70}$ (%): C, 50.73; H, 2.53; N, 3.70. Found (%): C, 50.12; H, 2.58; N, 3.72. IR (KBr, $cm^{-1}$): 3426.42 (s), 2971.57 (w), 1610.37 (m), 1531.77 (m), 1377.93 (s), 787.63 (w).

**Synthesis of $\{[Sr_3(HTCPP)_2]\cdot 6H_2O\}_n$ (4).** A mixture of **$H_4$TCPP** (0.05 mmol, 28.1 mg) and $SrCl_3\cdot 6H_2O$ (0.10 mmol, 12 mg) were dissolved in 14 mL of $CH_3CN/H_2O$ (4 : 3) in a 20 mL vial and heated in a Teflon-lined steel bomb at 160 °C for 4 days. Colorless crystals were collected in 57.0% yield (based on $H_4$TCPP). Anal. calcd. for $C_{64}H_{45}N_4O_{22}Sr_3(4)$ (%): C, 51.70; H, 3.19; N, 3.77. Found (%): C, 51.82; H, 3.22; N, 3.78. IR (KBr, $cm^{-1}$): 3436.46 (s), 1590.30 (m), 1387.96 (m), 1270.90 (s).

**Synthesis of $\{[Ce(HTCPP)]\cdot H_2O\}_n$ (5).** A mixture of **$H_4$TCPP** (0.05 mmol, 28.1 mg) and $CeCl_3\cdot 7H_2O$ (0.10 mmol, 37 mg) were dissolved in 14 mL of $CH_3CN/H_2O$ (4 : 3) in a 20 mL vial and heated in a Teflon-lined steel bomb at 160 °C for 4 days. Colorless crystals were collected in 57.0% yield (based on $H_4$-TCPP). Anal. calcd. for $C_{32}H_{19}N_2O_9Ce$ (%): C, 51.55; H, 2.30; N, 3.76. Found (%): C, 51.64; H, 2.38; N, 3.78. IR (KBr, $cm^{-1}$): 3436.46 (s), 1610.37 (m), 1531.77 (m), 1387.96 (s), 787.62 (w), 730.77 (w).

**Synthesis of $\{[Mn_2(TCPP)]\cdot 2.13H_2O\}_n$ (6).** A mixture of **$H_4$TCPP** (0.05 mmol, 28.1 mg) and $MnCl_2\cdot 6H_2O$ (0.10 mmol, 20 mg) were dissolved in 14 mL of $CH_3CN/H_2O$ (4 : 3) in a 20 mL vial and heated in a Teflon-lined steel bomb at 160 °C for 4 days. Light yellow crystals were collected in 43.0% yield (based on $H_4$TCPP). Anal. calcd. for $C_{32}H_{19}Mn_2N_2O_{10.13}$ (%): C, 57.68; H, 2.42; N, 4.20. Found (%): C, 57.72; H, 2.43; N, 4.24. IR (KBr, $cm^{-1}$): 3426.42 (s), 1657.19 (m), 1600.33 (s), 1531.77 (s), 1387.96 (s), 787.63 (w), 710.71 (w).

### Crystallographic data collection and refinement

The structural data of **1–6** were collected at 293/273 (K) on a Bruker SMART APEX-II CCD detector with graphite monochromatic Mo-Kα radiation ($\lambda$ = 0.71073 Å). All of the structures were solved by direct methods and refined with full-matrix least-squares procedures based on $F^2$ using SHELXS-97 and SHELXL 97 programs.[13] The non-hydrogen atoms were refined with anisotropic displacement parameters except for some free solvent molecules, and all the hydrogen atom positions were generated geometrically at idealized positions and refined by using a riding model. The topological analyses were performed using the TOPOS program.[14] Details of the crystal parameters, data collection, and refinements for compounds **1–6** are summarized in Table 1. The selected bond lengths and angles are listed in Table S1 in the ESI.†

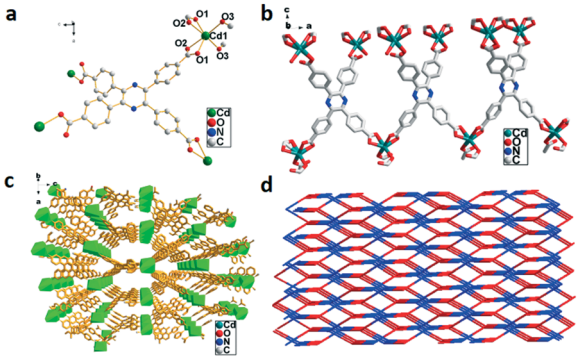


**Fig. 1** (a) Coordination environment of $Cd^{2+}$ in **1**, symmetry code: Cd1 = *x*, *y*, *z*; O2 = 1 − *x*, 0.25 + *y*, 0.25 + *z*. (b) 2D structure of **1** viewed along the *b* axis. (c) 3D framework of **1**. (d) 2-fold interpenetrated net of **1**.

## Results and discussion

### Crystal structure of $\{[Cd(H_2TCPP)]\cdot 2H_2O\}_n$ (1)

The X-ray structural analysis reveals that **1** belongs to the orthorhombic system with the space group *Fddd*. The asymmetric unit contains tetranuclear $Cd_4(TCPP)_4$ units. $Cd^{2+}$ centers are six-coordinated by six O atoms from four **$H_4$TCPP** molecules to form distorted octahedral geometries, as shown in Fig. 1a, with bond lengths in the range of 2.376(4)–2.240(4) similar to those reported in the literature.[11c,15] Each ligand coordinates to four $Cd^{2+}$ centers *via* two different modes to form a 2D network structure (Fig. 1b). An infinite 3D self-penetrating framework is further formed by the connection of bridge ligands and adjacent $Cd^{2+}$ centers with a layer distance of 11.4301(26) Å (Fig. 1c). The whole structure displays a 3D 2-fold interpenetrating 6-connected 4-c **sqc**182 net with a point symbol of $\{6^6\}\{6\cdot6\cdot6\cdot6(2)\cdot6(2)\cdot6(2)\}$ as illustrated in Fig. 1d.

### Crystal structure of $\{[Pb_2(TCPP)]\}_n$ (2)

The single-crystal X-ray diffraction analysis reveals that **2** crystallized in the triclinic system with the space group $P\bar{1}$. As shown in Fig. 2a, two coordination modes of $Pb^{2+}$ are observed in the asymmetric unit, in which Pb1 adopts a six-coordinated mode with six oxygen atoms from six **$H_4$TCPP** molecules, while Pb2 displays a five-coordinated mode with five oxygen atoms from four H4TCPP **molecules**. A parallelogram structure is formed by atoms O7–Pb1–O7–Pb1 in a clockwise direction with an angle ∠O7–Pb1–O7 of 78.828(3)°. Pb1 and Pb2 further connect with **$H_4$TCPP** to generate a 2D framework along the *a* axis containing two 1D nanosized quadrilateral channels with dimensions of 11.8775(7) Å × 12.5517(8) Å and 15.3615(10) Å × 11.7945(8) Å, respectively (Fig. 2b). The crystal accumulation diagram exhibits the formation of a hole in the cavity of complex **2** (Fig. 2c).

**Table 1** Crystallographic data of compounds **1–6**

| Complex | 1 | 2 | 3 | 4 | 5 | 6 |
|---|---|---|---|---|---|---|
| Formula | $C_{32}H_{16}CdN_2O_{10}$ | $C_{32}H_{16}N_2O_8Pb_2$ | $C_{32}H_{19}LaN_2O_{11.70}$ | $C_{64}H_{45}N_4O_{22}Sr_3$ | $C_{32}H_{19}CeN_2O_9$ | $C_{32}H_{19}Mn_2N_2$ $O_{10.13}$ |
| Mass | 700.87 | 970.85 | 757.6 | 1484.91 | 715.61 | 703.37 |
| Temperature/K | 293 K | 293 K | 293 K | 273 K | 293 K | 293 K |
| Crystal system | Orthorhombic | Triclinic | Triclinic | Triclinic | Triclinic | Orthorhombic |
| Space group | *Fddd* | $P\bar{1}$ | $P\bar{1}$ | $P\bar{1}$ | $P\bar{1}$ | *Pnna* |
| *a* (Å) | 12.850(4) | 9.9328(7) | 10.14(2) | 11.9979(14) | 10.124(2) | 19.677(7) |
| *b* (Å) | 18.906(6) | 11.8804(9) | 11.23(3) | 17.366(2) | 11.220(2) | 12.830(4) |
| *c* (Å) | 61.98(3) | 14.8808(10) | 15.24(3) | 17.573(2) | 15.330(3) | 30.250(11) |
| $\alpha$ (°) | 90 | 84.722(3) | 96.47(4) | 83.274(5) | 96.448(4) | 90 |
| $\beta$ (°) | 90 | 72.677(3) | 108.69(3) | 75.950(5) | 108.756(7) | 90 |
| $\gamma$ (°) | 90 | 87.758(3) | 98.73(5) | 82.588(4) | 98.885(7) | 90 |
| *V* (Å$^3$) | 15 058(9) | 1669.1(2) | 1601(6) | 3508.4(8) | 1604.4(6) | 7637(5) |
| *Z* | 16 | 2 | 2 | 2 | 2 | 8 |
| $D_{Calcd.}$ (g cm$^{-3}$) | 1.237 | 1.932 | 1.571 | 1.406 | 1.481 | 1.224 |
| *F* (000) | 5600 | 900 | 751 | 1494 | 710 | 2848 |
| GOOF | 1.030 | 1.074 | 1.063 | 1.315 | 1.226 | 1.033 |
| $\mu$ (mm$^{-1}$) | 0.629 | 10.122 | 1.399 | 2.346 | 1.472 | 0.711 |
| $R_{int}$ | 4.72% | 9.06% | 5.26% | 5.55% | 3.48% | 7.19% |
| $R_1$ $[I > 2\sigma(I)]^a$ | 0.0313 | 0.0350 | 0.0259 | 0.0529 | 0.0220 | 0.0861 |
| $wR_2$ (all data)$^b$ | 0.0797 | 0.0939 | 0.0645 | 0.1781 | 0.0742 | 0.2666 |

$^a$ $R_1 = \sum||F_o| - |F_c||/\sum|F_o|$. $^b$ $wR_2 = [\sum w(|F_o|^2 - |F_c|^2)^2/\sum w(F_o^2)^2]^{1/2}$.

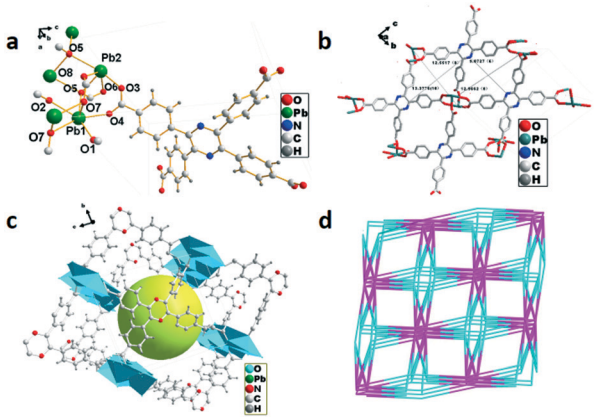

Fig. 2 (a) Coordination environment of $Pb^{2+}$ in **2**, symmetry code: Pb1 = *x*, *y*, *z*; O4 = −*x*, 1 − *y*, 1 − *z*. (b) 2D net structure of **2** with two 1D nanosized quadrilateral channels. (c) 3D framework of **2**. (d) Topology structure of **2**.

Topologically, the $H_4$TCPP ligand can be regarded as a 5,6-connected node, while $Pb^{2+}$ belongs to a 11-connected node. Therefore, the whole structure can be simplified as a 3-nodal (5,6,11)-connected topology with a Schläfli notation of $\{4^{10}\}\{4^{14}\cdot6\}\{4^{34}\cdot6^{21}\}$ as shown in Fig. 2d.

### Crystal structure of $\{[La(H_2TCPP)]\cdot3.7H_2O\}_n$ (3)

The single-crystal X-ray study reveals that **3** crystallized in the triclinic system with the space group $P\bar{1}$. A slightly disordered water molecule is observed which causes the non-integer number of oxygen atoms in the molecular formula, and meanwhile the hydrogen atoms cannot be obtained by Fourier differential peak synthesis. The asymmetric unit is composed of four $La^{3+}$ ions, four $H_4$TCPP molecules and one water molecule as displayed in Fig. 3a, in which $La^{3+}$ exhibits a distorted decahedral coordination configuration connected by eight oxygen atoms from $H_4$TCPP (La–O, 2.499(4)–2.673(5) Å) and one oxygen atom from water molecules (La–O, 2.531(4) Å). The adjacent $La^{3+}$ ions bonded to two $H_4$TCPP ligands form a dinuclear $\{La_2\}$ unit and two types of coordination modes can be observed: one employs a bidentate bridging coordination fashion $\mu_2$, while the other adopts a monodentate coordination mode *via* only an oxygen atom of the carboxylic group to a $La^{3+}$ ion. Further connection of dinuclear $\{La_2\}$ units with $H_4$TCPP ligands generates a 2D structure (Fig. 3b), which self-assembles into 3D networks (Fig. 3c). Topologically, **3** exhibits a 3D (4,8)-connecting 2-nodal 4,8-c net with stoichiometry $(4\text{-c})_2(8\text{-c})$ evaluated as an **sqc170** topology type, in which $La^{3+}$ is regarded as an 8-connector. Each $\{La_2\}$ unit is bonded to six $H_4$TCPP ligands, further connecting eight $\{La_2\}$ units, presenting an eight-connected **pcu** network with a point symbol of $\{4^{16}\cdot6^{12}\}\{4^4\cdot6^2\}_2$ (Fig. 3d).

### Crystal structure of $\{[Sr_3(HTCPP)_2]\cdot6H_2O\}_n$ (4)

The single-crystal X-ray analysis shows that **4** crystallized in the triclinic system with the space group $P\bar{1}$. Sr1 is linearly eight-coordinated by six oxygen atoms from four $H_4$TCPP molecules and two oxygen atoms from solvent water molecules with bond lengths of 2.508(2)–2.717(2) Å (Sr1–O) (Fig. 4a). Both Sr2 and Sr3 adopt a distorted octahedral geometry coordinated by four oxygen atoms from four $H_4$TCPP molecules and two oxygen atoms from solvent water molecules with bond lengths in the range of 2.518(2)–3.005(3)Å (Sr–O) (Fig. 4b). An attractive Sr-cam double helical chains can be observed in the left-handed (blue) and right-handed (violet) helical chains intertwined with each other along the *b* axis. The distances of two adjacent $Sr^{3+}$ centers were calculated to be 4.1101(4) Å and 3.9685(4) Å, respectively (Fig. 4c). Topologically, **4** can be rationalized as a 3-D (4,5,6,7,8)-connected network with a point symbol of $\{4^{10}\cdot6^5\}\{4^{12}\cdot6^9\}\{4^{18}\cdot6^{10}\}\{4^6\}\{4^7\cdot6^3\}$ in the case that $Sr^{3+}$ is regarded as an 8-connector (Fig. 4d).

### Crystal structure of $\{[Ce(HTCPP)]\cdot H_2O\}_n$ (5)

The X-ray structural analysis reveals that **5** crystallized in the triclinic system with the space group $P\bar{1}$. The asymmetric unit

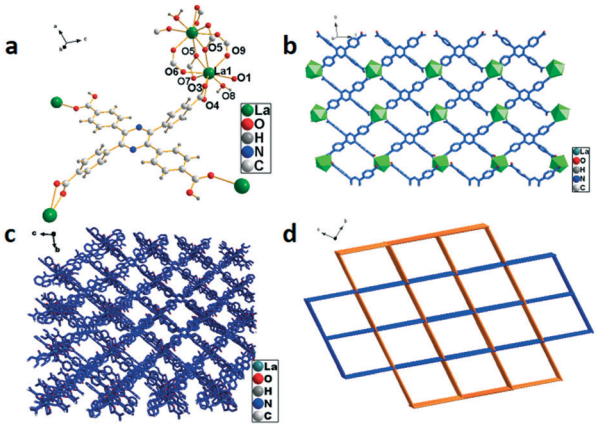

Fig. 3 (a) Coordination environment of $La^{3+}$ in **3**, symmetry code: La1 = *x*, *y*, *z*; O5 = *x*, *y*, *z*. (b) 2D structure of **3**. (c) Crystal accumulation diagram of **3**. (d) Topology structure of **3**.

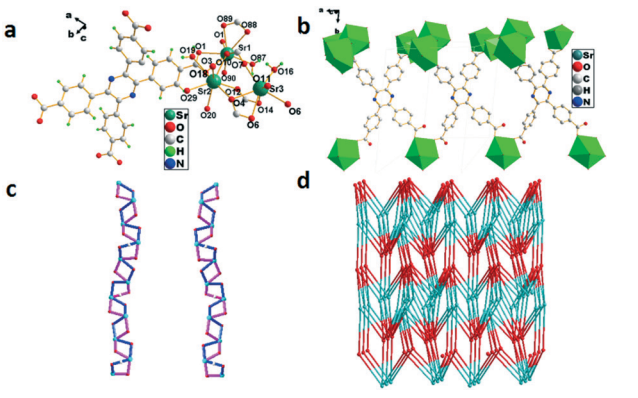

Fig. 4 (a) Coordination environment of $Sr^{3+}$ in **4**, symmetry code: Sr1 = *x*, 1 + *y*, *z*; Sr2 = 1 − *x*, 1 − *y*, 1 − *z*. (b) $Sr^{3+}$ ion polyhedral diagram of **4**. (c) The left-and right-handed helical chains of Sr-cam. (d) 3D 5-nodal (4,5,6,7,8)-connected topological network.

contains two $Ce^{3+}$ ions, one $H_4TCPP$ molecule and a water molecule, as shown in Fig. 5a. $Ce^{3+}$ ions adopt a nine-coordinated mode to form a distorted decahedron, in which $Ce^{3+}$ is surrounded by eight oxygen atoms from six $H_4TCPP$ molecules and another oxygen atom from a water molecule. A binuclear cluster unit (Ce1–O4–Ce1–O4) forms by the connection of two Ce atoms *via* two oxygen atom (O4) bridges, and the distance of Ce(1)···Ce(1) is 4.1223(9) Å. The $H_4TCPP$ connects four Ce(III) ions and the adjacent Ce(III) ions are bridged by two $H_4TCPP$ molecules so as to form 2D-cavity with sizes of *ca.* 10.3113(17) Å × 15.3304(25) Å and 12.9555(20) Å × 12.8338(21) Å along the *b* axis, respectively (Fig. 5b). The $\{Ce_2\}$ units further connect with another two $H_4TCPP$ molecules to form a 3D porous structure as shown in Fig. 5c. Topological analysis suggests that **5** exhibits a uninodal 8-connected 20-c net topology with a point symbol of $\{3^{78}\cdot4^{98}\cdot5^{14}\}$ (Fig. 5d).

### Crystal structure of $\{[Mn_2(TCPP)]\cdot2.13H_2O\}_n$ (6)

The single-crystal X-ray diffraction analysis reveals that **6** crystallized in the monoclinic system with the space group *Pnna*. The non-integer number of the oxygen atom in molecule **6** can be ascribed to the same reason as that depicted in **3**. The asymmetric unit contains two Mn(II) ions and one $H_4TCPP$ molecule to form a distorted octahedral fashion, which consists of six oxygen atoms from four $H_4TCPP$ molecules with Mn–O bond lengths in the range of 2.027–2.319 Å (Fig. 6a). The deprotonated carboxylic acid group of $H_4TCPP$ coordinates to $Mn^{2+}$ ions *via* two different modes resulting in the formation of a ladder-shaped network, in which the two helical chains and ligands were seen as banisters and staircases, respectively (Fig. 6b). Each 2D chain interacts with neighboring chains *via* the $H_4TCPP$ ligand, which further extends the 2D framework to a 3D supramolecular framework (Fig. 6c). Topologically, the whole structure can be simplified as a 3,4,4,5,17-connected net with a point symbol of $\{4\cdot5^2\}_2\{4^{32}\cdot5^6\cdot6^{84}\cdot7^4\cdot8^{10}\}\{4^5\cdot5\}\{4^6\}\{4^8\cdot5^2\}$ (Fig. 6d).

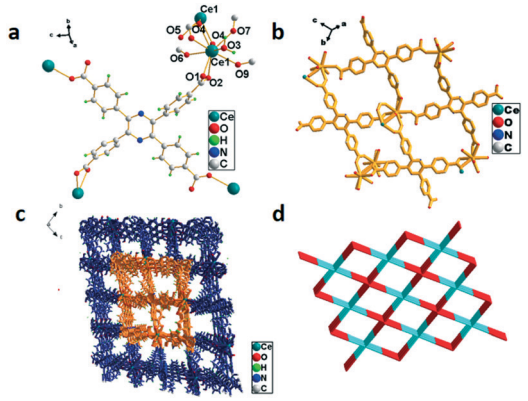


**Fig. 5** (a) Coordination environment of $Ce^{3+}$ in **5**, symmetry code: Ce1 = *x*, *y*, *z*; O1 = *x*, *y*, 1 + *z*. (b) 2D structure of **5**. (c) The 3D framework of **5**. (d) 3D 8-connected topological network.

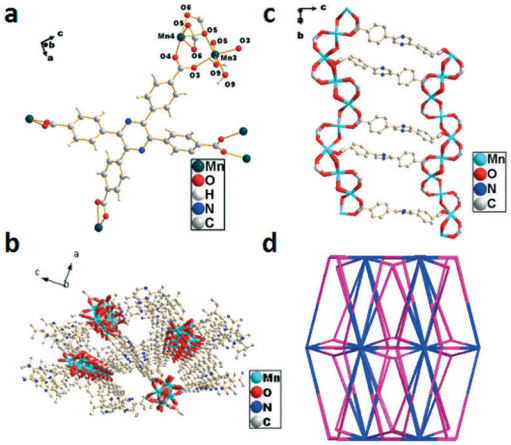


**Fig. 6** (a) Coordination environment of $Mn^{2+}$ in **6**, the hydrogen atoms are omitted for clarity, symmetry code: Mn3 = *x*, *y*, *z*; Mn4 = *x*, *y*, *z*. (b) Double-helix chain of **6**. (c) Views of the 3D framework of **6** along the *b* axis. (d) Topological structure of **6**.

### PXRD, thermogravimetric analysis and adsorption properties

PXRD shows that the peak positions of the obtained crystal samples of **1–6** are in excellent agreement with the simulated peak positions from the single crystal data, which indicates the phase purity of the synthesized samples (Fig. S7–Fig. S12†). TG on **1–6** was investigated in the temperature range of 0–600 °C (Fig. S13†). The thermogravimetric curve displays that **1** decomposes in three obvious weight loss steps, including the initial weight loss of 7.6% from 0–160 °C ascribed to residual water molecules in the crystal, the weight loss of 4.4% (calcd 4.5%) of two coordinated water molecules from 160–440 °C and the weight loss at around 440 °C for structural decomposition of the MOF framework. **2** lost one lattice water molecule from 0 to 100 °C with a weight loss of 1.4% (calcd. 1.6%), and then remained thermally stable till 430 °C without any weight loss. **3** lost one lattice water molecule from 0–102 °C with a weight loss of 2.2% (calcd. 2.3%) and two coordinated water molecules at 102–420 °C with a weight loss of 4.2% (calcd. 4.4%), and then began to collapse at around 420 °C. **4** exhibited a weight loss of 2.6% (calcd. 3.0%) from 0–400 °C corresponding to three coordinated water molecules. **5** lost one coordinated water molecule from 0–200 °C with a weight loss of 2.1% (calcd. 2.2%), and then remained thermally stable till 432 °C. **6** presented a weight loss of 4.8% (calcd. 5.1%) ascribed to two lattice water molecules from 120–430 °C, then the whole structure began to collapse at around 430 °C. The thermogravimetric analyses suggest that all MOFs exhibit excellent thermal stability. Subsequently, the porosity of **1–6** was investigated *via* $N_2$ adsorption at 77 K. As shown in Fig. S14,† **3** and **6** achieve saturated $N_2$ uptake values of 46 and 40 $cm^3\ g^{-1}$ (STP), and the calculated Brunauer–Emmett–Teller (BET) surface areas are 18.325 $m^2\ g^{-1}$ and 31.128 $m^2\ g^{-1}$, respectively. The experimental total pore volumes for **3** and **6** were calculated to be 0.06396 $cm^3\ g^{-1}$ and 0.07064 $cm^3\ g^{-1}$, respectively. However, the other MOFs showed relatively poor performance in $N_2$

 

adsorption, which could be mainly ascribed to their BET surface areas and pore volumes, and the corresponding data are listed in Table S2.†

### Optical properties and NAC sensing

The UV/vis and emission spectra of all MOFs as well as the ligand **$H_4$TCPP** were investigated in the solid state at room temperature (Fig. S15 and S16†). As can be seen in the UV-vis absorption spectra, **$H_4$TCPP** and complexes **1–6** showed similar absorption bands in the UV regions of 220–310 nm and 310–400 nm, which could be ascribed to the π–π* transition between ligands and metal-to-ligand charge-transfer (MLCT) transitions.[16] In addition, the solid state fluorescence spectra of **1–6** as well as **$H_4$TCPP** are shown in Fig. S16.† The results indicated that compound **$H_4$TCPP** exhibited the maximum emission band centered at 467 nm, while the maximum emissions of compounds **1–4** showed obvious blue shifts compared to that of **$H_4$TCPP**, which may be assigned to the intraligand π–π* or n–π* transition.[11a,17] However, compounds **5** and **6** show no obvious characteristic emission peak, which may be ascribed to several factors, such as different coordination modes, coordination environments of metal ions and rigid solid-state crystal packing.[18]

Subsequently, all MOFs were further explored for sensing nitro-aromatic compounds (NACs), a class of highly toxic and explosive materials. The fluorescence sensing performance of MOFs **1–6** towards various NACs was investigated by the addition of identical amounts of NACs, such as 2-nitroaniline (2-NA), 4-nitroaniline (4-NA), 2-nitrophenol (2-NP), 4-nitrophenol (4-NP), nitrobenzene (NB), 2,4-dinitrophenol (2,4-DNP), 2,4-dinitrophenylhydrazine (2,4-DNPH) and picric acid (TNP) to various MOFs dispersed in water. As shown in Fig. 7a, all MOFs showed high selectivity to TNP with ratios of fluorescence quenching in the range of 87–100%, whereas they exhibited relatively poor selectivity to 2-NP and NB with the maximum ratio of fluorescence quenching of 84.8% and 71.8%, respectively. The selectivity may be contributed to the interactions between the open nitrogen atoms in the pyrazine unit and the free acid sites (amino or hydroxyl) of NACs as well as the electron and energy transfer between the electron-deficient TNP and fluorophore.[10a,12,19] In order to further compare the efficiency of various sensors, fluorescence titrations were carried out with gradual addition of TNP to various MOFs dispersed in water as depicted in Fig. S17,† and the Stern–Volmer (SV) equation, $(I_0/I) = K_{sv}[A] + 1$, where $I_0$ is the initial fluorescence intensity before the addition of an analyte, $I$ is the fluorescence intensity in the presence of the analyte, $[A]$ is the molar concentration of the analyte, and $K_{sv}$ is the quenching constant ($M^{-1}$), was utilized to evaluate the fluorescence quenching efficiency so as to compare the efficiency of the different MOFs (Fig. 7b). At very low concentrations of TNP, a linear increase in the SV plot was observed, which diverged from linearity and began to bend upwards upon further increasing the concentration. This non-linear nature of the SV plots for TNP suggests the probable mechanism of a combination of static and dynamic quenching processes or an energy transfer phenomenon between TNP and MOFs.[19c–e] Based on the equation, the quenching constants ($K_{sv}$) of MOFs **1–6** for TNP can be estimated to be $8.5 \times 10^4$ $M^{-1}$, $1.8 \times 10^5$ $M^{-1}$, $1.3 \times 10^5$ $M^{-1}$, $2.2 \times 10^5$ $M^{-1}$, $1.2 \times 10^5$ $M^{-1}$, and $1.6 \times 10^5$ $M^{-1}$, respectively (Fig. S18†). However, all the quenching constants are larger than those of a previously reported pyrazine-based MOF sensor.[12] As mentioned above, the pyrazine-based MOFs show highly selective fluorescence quenching towards NACs, especially TNP.

### Electrocatalytic performances toward the HER

The HER catalytic activities of **$H_4$TCPP** and **1–6** were evaluated by LSV reaching negative potentials down to −1 V *vs.* Ag/AgCl.[20] These experiments were conducted in 1 M KOH aqueous solution (pH = 14) using an RDE rotating at 1200 rpm in a standard three-electrode mode with a scan rate of 5 mV $s^{-1}$. The catalyst-based working electrode was obtained through loading the as-prepared samples onto the surface of the GCE.[21] The polarization curves of the as-prepared catalyst were obtained by LSV measurements and presented in Fig. 8a. As expected, the electrocatalytic activities of the tested MOFs were obviously improved compared to that of ligand **$H_4$TCPP**. In particular, **2** and **5** presented markedly enhanced electrocatalytic performances with onset overpotentials of 362 and 244 mV, and achieved a current density of 10 mA $cm^{-2}$ ($j_{10}$) at overpotentials of 449 mV and 457 mV, respectively. The corresponding data of **$H_4$TCPP** and **1–6** are listed in Table S3.† To further demonstrate the stability of MOFs under test conditions, **2** and **5** were chosen to be

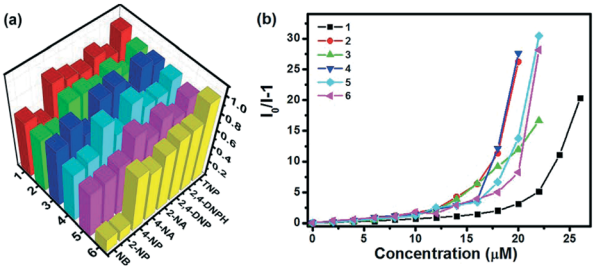


Fig. 7 (a) Fluorescence quenching efficiencies of MOFs **1–6** (0.5 mg in 2 mL $H_2O$) towards various NACs (30 μM); (b) Stern–Volmer (SV) plots of MOFs **1–6** (0.5 mg in 2 mL $H_2O$) for TNP.

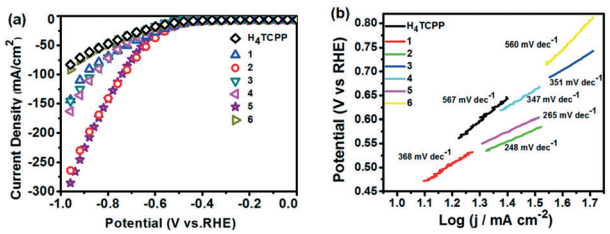


Fig. 8 (a) HER polarization curves of **$H_4$TCPP** and compounds **1–6** in 1 M KOH solution with a scan rate of 5 mV $s^{-1}$. (b) Tafel plots of **$H_4$TCPP** and compounds **1–6**.

immersed in 1 M KOH aqueous solution at different times and the corresponding PXRD patterns were recorded. As shown in Fig. S19 and S20,† the PXRD profiles of **2** and **5** were almost unaltered after 4 hours of immersion, revealing the retained crystallinity, which suggested the stability of MOFs under test conditions. The HER kinetics of the tested samples were obtained using the corresponding Tafel plots *via* fitting the linear regions to the Tafel equation ($\eta = b \log j + \alpha$, $\eta$ for the overpotential, $b$ for the Tafel slope, $j$ for the current density, and $\alpha$ for the Tafel constant). Particularly, the Tafel slopes of **2** and **5** were obtained to be *ca.* 248 and 265 mV dec$^{-1}$, respectively, which were much smaller than that of the **$H_4$TCPP** (567 mV dec$^{-1}$), suggesting more favorable kinetics towards the electrocatalytic HER (Fig. 8b). Subsequently, electrochemical impedance spectroscopy (EIS) was employed to investigate the electrode kinetics under the catalytic HER operating conditions. The Nyquist plots (Fig. S21†) revealed the obviously reduced charge transfer resistance of **2** and **5** in comparison with that of other MOFs and ligand **$H_4$TCPP**, which also suggested a faster electron transfer process and facile kinetics toward the hydrogen evolution involving the catalyst **2** or **5**.

## Conclusions

In summary, we herein presented a series of new MOFs with 3D porous networks based on the backbone of tetracarboxylic acid derived from pyrazine. All MOFs were characterized by single-crystal X-ray diffraction, powder X-ray diffraction, elemental analysis, IR spectroscopy, thermal-gravimetric analysis and fluorescence spectroscopy. In addition, almost all MOFs exhibited sensitive response to NACs, especially to TNP, with fluorescence quenching efficiency behaviors. Remarkably, MOFs **2** and **5** exhibited a certain activity on the electrocatalytic HER without conductive additives or other binders with Tafel slopes of 248 and 265 mV dec$^{-1}$, respectively. The results indicate that neat MOFs exhibit promising electrocatalytic performances in the HER, which may provide a new avenue for exploring MOF materials in electrocatalytic materials.

## Conflicts of interest

There are no conflicts to declare.

## Acknowledgements

This work was financially supported by the National Natural Science Foundation of China (21671159), the Meritocracy Research Funds of China West Normal University (17YC030) and the Key Laboratory of Chemical Synthesis and Pollution Control of Sichuan Province (CSPC201802).

## Notes and references

1 (*a*) P. Horcajada, R. Gref, T. Baati, P. K. Allan, G. Maurin, P. Couvreur, G. Férey, R. E. Morris and C. Serre, *Chem. Rev.*, 2012, **112**, 1232; (*b*) H. Furukawa, K. E. Cordova, M. O'Keeffe and O. M. Yaghi, *Science*, 2013, **341**, 1230444; (*c*) J. Pang, S. Yuan, J. Qin, C. Liu, C. Lollar, M. Wu, D. Yuan, H. C. Zhou and M. C. Hong, *J. Am. Chem. Soc.*, 2017, **139**, 16939; (*d*) H. L. Wang, Q. L. Zhu, R. Zou and Q. Xu, *Chem*, 2017, **2**, 52; (*e*) X. Gu and D. Xue, *CrystEngComm*, 2007, **9**, 471.

2 (*a*) K. M. L. Taylor-Pashow, J. Della Rocca, Z. Xie, S. Tran and W. B. Lin, *J. Am. Chem. Soc.*, 2009, **131**, 14261; (*b*) J. R. Li, J. Sculley and H. C. Zhou, *Chem. Rev.*, 2012, **112**, 869; (*c*) W. J. Ma, Q. Jiang, P. Yu, L. F. Yang and L. Q. Mao, *Anal. Chem.*, 2013, **85**, 7550; (*d*) T. Zhang and W. Lin, *Chem. Soc. Rev.*, 2014, **43**, 5982; (*e*) Z. Hu, B. J. Deibert and J. Li, *Chem. Soc. Rev.*, 2014, **43**, 5815; (*f*) S. S. Nagarkar, A. V. Desai and S. K. Ghosh, *CrystEngComm*, 2016, **18**, 2994; (*g*) M. X. Wu and Y. W. Yang, *Adv. Mater.*, 2017, **29**, 1606134; (*h*) K. Tanaka, K. Sakuragi, H. Ozaki and Y. Takada, *Chem. Commun.*, 2018, **54**, 6328.

3 (*a*) N. S. Lewis and D. G. Nocera, *Proc. Natl. Acad. Sci. U. S. A.*, 2006, **103**, 15729; (*b*) M. Balat and H. Balat, *Energy Sources, Part A*, 2009, **31**, 1280; (*c*) T. R. Cook, D. K. Dogutan, S. Y. Reece, Y. Surendranath, T. S. Teets and D. G. Nocera, *Chem. Rev.*, 2010, **110**, 6474; (*d*) D. Merki and X. Hu, *Energy Environ. Sci.*, 2011, **4**, 3878.

4 (*a*) M. S. Dresselhaus and I. L. Thomas, *Nature*, 2001, **414**, 332; (*b*) J. A. Turner, *Science*, 2004, **305**, 972.

5 (*a*) P. Xiao, M. A. Sk, L. Thia, X. Ge, R. J. Lim, J. Y. Wang, K. H. Lim and X. Wang, *Energy Environ. Sci.*, 2014, **7**, 2624; (*b*) J. Tian, N. Cheng, Q. Liu, W. Xing and X. Sun, *Angew. Chem., Int. Ed.*, 2015, **54**, 5493; (*c*) M. R. Gao, J. X. Liang, Y. R. Zheng, Y. F. Xu, J. Jiang, Q. Gao, J. Li and S. H. Yu, *Nat. Commun.*, 2015, **6**, 5982; (*d*) W. Salomon, G. Paille, M. Gomez-Mingot, P. Mialane, J. Marrot, C. Roch-Marchal, G. Nocton, C. Mellot-Draznieks, M. Fontecave and A. Dolbecq, *Cryst. Growth Des.*, 2017, **17**, 1600.

6 H. Kita, *J. Electrochem. Soc.*, 1966, **113**, 1095.

7 (*a*) R. Kitaura, S. Kitagawa, Y. Kubota, T. C. Kobayashi, K. Kindo, Y. Mita, A. Matsuo, M. Kobayashi, H. C. Chang, T. C. Ozawa, M. Suzuki, M. Sakata and M. Takata, *Science*, 2002, **298**, 2358; (*b*) S. Yang, X. Lin, A. J. Blake, G. S. Walker, P. Hubberstey, N. R. Champness and M. Schröder, *Nat. Chem.*, 2009, **1**, 487; (*c*) Y. He, W. Zhou, G. Qian and B. Chen, *Chem. Soc. Rev.*, 2014, **43**, 5657; (*d*) J. Mehta, N. Bhardwaj, S. K. Bhardwaj, K. H. Kim and A. Deep, *Coord. Chem. Rev.*, 2016, **322**, 30.

8 (*a*) A. Mahmood, W. Guo, H. Tabassum and R. Zou, *Adv. Energy Mater.*, 2016, **6**, 1600423; (*b*) H. M. Barkholtz and D. J. Liu, *Mater. Horiz.*, 2017, **4**, 20; (*c*) K. Shen, X. Chen, J. Chen and Y. Li, *ACS Catal.*, 2016, **6**, 5887; (*d*) Z. Song, N. Cheng, A. Lushington and X. Sun, *Catalysts*, 2016, **6**, 116; (*e*) H. Zhang, H. Osgood, X. Xie, Y. Shao and G. Wu, *Nano Energy*, 2017, **31**, 331.

9 D. Sheberla, J. C. Bachman, J. S. Elias, C. J. Sun, Y. Shao-Horn and M. Dincă, *Nat. Mater.*, 2017, **16**, 220.

10 (*a*) S. S. Nagarkar, B. Joarder, A. K. Chaudhari, S. Mukherjee and S. K. Ghosh, *Angew. Chem.*, 2013, **125**, 2953; (*b*) C. Zhang, Y. Yan, L. Sun, Z. Liang and J. Li, *CrystEngComm*, 2016, **18**, 4102; (*c*) L. Zhang, Z. Kang, X. Xin and D. Sun,

 

*CrystEngComm*, 2016, **18**, 193; (*d*) Y. T. Yan, J. Liu, G. P. Yang, F. Zhang, Y. K. Fan, W. Y. Zhang and Y. Y. Wang, *CrystEngComm*, 2018, **20**, 477.

11 (*a*) W. Y. Guan, F. Xiong, H. L. Zhang, W. Tang, S. F. Zhang, L. H. Jing and D. B. Qin, *CrystEngComm*, 2014, **16**, 7701; (*b*) S. F. Zhang, F. Xiong, Z. He, Y. Liang, J. R. Xue, L. H. Jing and D. B. Qin, *Polyhedron*, 2015, **102**, 401; (*c*) Y. Liang, W. G. Yuan, S. F. Zhang, Z. He, J. R. Xue, X. Zhang, L. H. Jing and D. B. Qin, *Dalton Trans.*, 2016, **45**, 1382.

12 Y. Jiang, L. Sun, J. Du, Y. Liu, H. Shi, Z. Liang and J. Li, *Cryst. Growth Des.*, 2017, **17**, 2090.

13 (*a*) G. M. Sheldrick, *SHELXS 97, Program for Crystal Structure Solution*, University of Göttingen, Göttingen, Germany, 1997; (*b*) G. M. Sheldrick, *SHELXL 97, Program for Crystal Structure Refinement*, University of Göttingen, Göttingen, Germany, 1997.

14 V. A. Blatov, A. P. Shevchenko and V. N. Serezhkin, *J. Appl. Crystallogr.*, 2000, **33**, 1193.

15 (*a*) D. Singh and C. M. Nagaraja, *Cryst. Growth Des.*, 2015, **15**, 3356; (*b*) Z. Ju, W. Yan, X. Gao, Z. Shi, T. Wang and H. Zheng, *Cryst. Growth Des.*, 2016, **16**, 2496.

16 (*a*) J. S. Hu, Y. J. Shang, X. Q. Yao, L. Qin, Y. Z. Li, Z. J. Guo, H. G. Zheng and Z. L. Xue, *Cryst. Growth Des.*, 2010, **10**, 4135; (*b*) Z. L. Fang, R. M. Yu, J. G. He, Q. S. Zhang, Z. G. Zhao and C. Z. Lu, *Inorg. Chem.*, 2009, **48**, 7691.

17 (*a*) Z. Z. Lin, F. L. Jiang, L. Chen, C. Y. Yue, D. Q. Yuan, A. J. Lan and M. C. Hong, *Cryst. Growth Des.*, 2007, **7**, 1712; (*b*) P. Cui, Z. Chen, D. L. Gao, B. Zhao, W. Shi and P. Cheng, *Cryst. Growth Des.*, 2010, **10**, 4370; (*c*) X. J. Li, Z. J. Yu, T. Guan, X. X. Li, G. C. Ma and X. F. Guo, *Cryst. Growth Des.*, 2015, **15**, 278.

18 A. Wozna and A. Kapturkiewicz, *Phys. Chem. Chem. Phys.*, 2015, **17**, 30468.

19 (*a*) M. Wang, V. Vajpayee, S. Shanmugaraju, Y. R. Zheng, Z. Zhao, H. Kim, P. S. Mukherjee, K. W. Chi and P. J. Stang, *Inorg. Chem.*, 2011, **50**, 1506; (*b*) S. Dalapati, S. Jin, J. Gao, Y. Xu, A. Nagai and D. Jiang, *J. Am. Chem. Soc.*, 2013, **135**, 17310; (*c*) S. S. Nagarkar, A. V. Desai and S. K. Ghosh, *Chem. Commun.*, 2014, **50**, 8915; (*d*) B. Joarder, A. V. Desai, P. Samanta, S. Mukherjee and S. K. Ghosh, *Chem. – Eur. J.*, 2015, **21**, 965; (*e*) S. Khatua, S. Goswami, S. Biswas, K. Tomar, H. S. Jena and S. Konar, *Chem. Mater.*, 2015, **27**, 5349.

20 Z. Xiao, Y. Wang, S. Zhang, W. Fan, X. Xin, X. Pan, L. Zhang and D. Sun, *Cryst. Growth Des.*, 2017, **17**, 4084.

21 (*a*) Y. P. He, Y. X. Tan and J. Zhang, *Cryst. Growth Des.*, 2013, **13**, 6; (*b*) L. Wang, Y. Wu, R. Cao, L. Ren, M. Chen, X. Feng, J. Zhou and B. Wang, *ACS Appl. Mater. Interfaces*, 2016, **8**, 16736.